Improved atomistic Monte Carlo models based on *ab − initio* -trained neural networks: Application to FeCu and FeCr alloys

N. Castin, L. Messina, C. Domain, R. Pasianot, P. Olsson

Improved atomistic Monte Carlo models based on *ab-initio*-trained neural networks: Application to FeCu and FeCr alloys

N. Castin,[1,*] L. Messina,[2] C. Domain,[3] R. C. Pasianot,[4] and P. Olsson[5]

[1]*Studie Centrum voor Kerneenergie - Centre d'Études de l'énergie Nucléaire (SCK•CEN), NMS unit, Boeretang 200, B2400 Mol, Belgium*

[2]*DEN-Service de Recherches de Métallurgie Physique, CEA, Université Paris-Saclay, F-91191 Gif-sur-Yvette, France*

[3]*Département Matériaux et Mécanique des Composants, EDF-R&D, Les Renardières, F-77250 Moret sur Loing, France*

[4]*Gerencia Materiales, Comisión Nacional de Energía Atómica (CNEA), Avenida General Paz 1499, 1650 San Martín, Argentina, and CONICET*

[5]*KTH Royal Institute of Technology, Reactor Physics, Roslagstullsbacken 21, 106 91 Stockholm, Sweden*

(Received 20 October 2016; revised manuscript received 11 May 2017; published 29 June 2017)

We significantly improve the physical models underlying atomistic Monte Carlo (MC) simulations, through the use of *ab initio* fitted high-dimensional neural network potentials (NNPs). In this way, we can incorporate energetics derived from density functional theory (DFT) in MC, and avoid using empirical potentials that are very challenging to design for complex alloys. We take significant steps forward from a recent work where artificial neural networks (ANNs), exclusively trained on DFT vacancy migration energies, were used to perform kinetic MC simulations of Cu precipitation in Fe. Here, a more extensive transfer of knowledge from DFT to our cohesive model is achieved via the fitting of NNPs, aimed at accurately mimicking the most important aspects of the *ab initio* predictions. Rigid-lattice potentials are designed to monitor the evolution during the simulation of the system energy, thus taking care of the thermodynamic aspects of the model. In addition, other ANNs are designed to evaluate the activation energies associated with the MC events (migration towards first-nearest-neighbor positions of single point defects), thereby providing an accurate kinetic modeling. Because our methodology inherently requires the calculation of a substantial amount of reference data, we design as well lattice-free potentials, aimed at replacing the very costly DFT method with an approximate, yet accurate and considerably more computationally efficient, potential. The binary FeCu and FeCr alloys are taken as sample applications considering the extensive literature covering these systems.

DOI: 10.1103/PhysRevB.95.214117

I. INTRODUCTION

Monte Carlo (MC) methods [1–4] are widespread tools to describe diffusion-controlled phenomena at the atomic level. They are suitable to study a wide variety of materials up to experimentally relevant length and time scales, shedding light on the resulting microstructural and microchemical evolution during operational conditions, e.g., under irradiation [5–7]. Generally based on a rigid-lattice approach, they feature an explicit spatial characterization of the diffusion of lattice defects and atoms, allowing for a detailed investigation of the kinetics of formation of fine microstructural features. For instance, kinetic MC methods (KMCs) have been widely employed to characterize steels under irradiation [7–9], in particular the formation of embrittling solute-defect clusters [10–12]. While these methods are in principle well suited for the investigation of the underlying atomic-scale mechanisms, the task is extremely challenging due to the chemical complexity of the reference alloys. Specifically, in atomistic KMCs (AKMCs), the evolution of the alloy proceeds through migration events of single defects (vacancies and/or interstitials) [1,13,14], which are stochastically selected at each step based on their transition rates. The accuracy of the latter parameters is thus crucial to ensure the physical reliability of the model, as they embody both thermodynamics and kinetics properties of the system being studied.

Migration rates associated with single point defects are traditionally computed with several approaches (see, e.g., Refs. [15,16] for extensive reviews). Some are based on first-principles methods such as density functional theory (DFT) [17,18], while others rely on system-specific interatomic potentials (IAPs) [2,4]. In any case, suitable mathematical frameworks are necessary to predict the energies associated with each atomic configuration, as well as the migration frequencies associated with each transition event that may be encountered during the simulation. Such frameworks are usually cohesive models based on pair-interaction [2,19] or cluster-expansion methods [18], and supported by limited data sets of experimental and *ab initio* properties. Their range of applicability is thus limited by their intrinsic rigid-lattice framework and by their poor transferability to new kinds of configurations beyond their original intended scope. IAPs, on the other hand, provide a general framework to describe any stable or metastable configuration, even allowing for the portability to lattice-free MC models [20–23]. Nevertheless, their direct "on-the-fly" use as cohesive models in classical rigid-lattice MC is impractical, because the exact saddle-point configurations in each transition event are unknown and must be sought with time-consuming procedures.

In previous works [24–26], we showed how machine-learning techniques, specifically artificial neural networks (ANNs), can improve the physical parametrization of AKMC simulations. Consistently with the above-discussed objectives, these ANNs were designed to predict the migration energies associated with single point defects in binary Fe-Cu and Fe-Cr alloys, as calculated without approximation using a given IAP

*nicolas.m.b.castin@gmail.com

under the embedded atom method (EAM) formalism. This first-of-a-kind approach maximized the transfer of physical information across increasing modeling scales within reasonable computational times, because no static property stemming from the reference cohesive model needed to be discarded. It is worth noting that the choice to rely on EAM potentials was mainly dictated by the necessity of producing large numbers of migration barriers (tens of thousands) required for an accurate fitting of the ANNs. On the other hand, developing IAPs for more complex alloys is a challenging task, and has to be tailored each time to the specific system under investigation. Given the inherent simplicity and the limited variable parameters, the underlying mathematical framework in EAM-like formalisms is undoubtedly insufficient to encompass the whole set of thermodynamic and kinetic properties of the alloy. IAPs are therefore always targeted on some properties, at the expense of others (see, e.g., Ref. [27]). In this sense, the substitution of IAPs with DFT would considerably improve the physical reliability of KMC simulations, as DFT provides a more comprehensive (although not always necessarily accurate) description of the alloy. The combination of DFT with powerful ANN-based regression schemes can thus potentially provide a breakthrough improvement of the KMC physical models.

The application of neural networks is nowadays more and more common in many fields of science (see, e.g., Ref. [28]), especially where hidden relationships must be searched among large amounts of data in complex systems. In the field of materials modeling, specifically, several methodologies have been proposed to perform large-scale molecular dynamics (MD) simulations using ANN-based cohesive models exclusively fitted on DFT properties. For instance, Behler and co-workers (see, e.g., Refs. [29–31]) elaborated strategies for constructing high-dimensional neural network potentials (NNPs). Csányi and co-workers (see, e.g., Refs. [32,33]) achieved equivalent goals by developing mathematically different concepts based on Gaussian approximation networks. The application of these methods to MC simulations allows for the transfer of accurate electronic-scale properties to even larger scales than MD, as suggested in Ref. [34] and achieved in Ref. [35].

Given the central role played by migration barriers in AKMC simulations, a logical first step is to target their accurate prediction by means of suited ANNs. This was the approach pursued in a recent work [36], where the coherent precipitation of copper in iron was investigated in the framework of a hybrid KMC model. The latter was powered by an ANN trained on an extensive database of single-vacancy migration rates obtained with DFT. This represented an attempt to introduce fully DFT-based energy functions implemented with ANNs in KMC simulations. In comparison with our previous works based on an EAM potential [25], the model led to a considerable improvement of the time scale matching with thermal-ageing experiments, but presented two main limitations: the lack of leverage on thermodynamic properties (which did not allow for a correction of the faulty DFT solubility limit), and the limited size of the supercell used for DFT calculations that did not allow for the treatment of vacancy migration events next to large solute clusters in the late precipitation stages.

This work aims at addressing these limitations by developing full NNP cohesive models, in order to go beyond the exclusive prediction of migration barriers. To this purpose, two kinds of NNPs are developed. (a) The first is rigid-lattice NNPs aimed at evaluating the energies associated with stable configurations, thus providing an accurate thermodynamic description of the alloy. This contribution may be included in AKMC models, as well as in Metropolis Monte Carlo (MMC) calculations [37]. (b) The second is lattice-free NNPs specifically designed to perform static calculations. Their intended application is the calculation of equilibrium and saddle-point energies for MC simulations. As described in Sec. II, we benefit from the state-of-the-art techniques proposed by the above-mentioned authors, and we adapt them to the specific purposes of our study. For this purpose, NNP training is focused on energy prediction only, since this is the most essential information to transfer from DFT to atomistic (kinetic) Monte Carlo models. We demonstrate it in Sec. III for the binary Fe-Cu and Fe-Cr systems.

II. HIGH-DIMENSIONAL NEURAL NETWORK POTENTIALS

In this section, we present our method to design DFT-based high-dimensional neural network potentials (NNPs), targeting specific properties and qualities as required for rigid-lattice Monte Carlo models. As already stated, our methodology is based on the work of Behler, Csányi, and co-authors. In complement to the already cited references, interested readers are directed to tutorial reviews in Refs. [38,39] and references therein for an extensive description of the state of the art. In these references, NNPs are mostly designed for the purpose of performing MD simulations, and their fitting is thus in general achieved including energy- and force-matching criteria. Considering our target scale (MMC and AKMC), and specifically the rigid-lattice character of the models, we opt for an energy-matching strategy. We start, in Sec. II A, by defining the concepts of rigid-lattice and lattice-free potentials. The key feature for managing the NNP behavior resides in a proper choice of the ANN input variables, describing the atomic structures, as discussed in Sec. II B. Next, NNP fitting is discussed in Sec. II C. Finally, our strategy to produce adequate databases of training data is described in Sec. II D.

A. Rigid-lattice and lattice-free potentials

Similarly to any interatomic potential, NNPs provide a mathematical tool for assigning a total energy and individual forces to atomic configurations, as functions of the coordinates in space and the chemical species associated with every individual particle at play. They are thus fully functional for static calculations, such as the relaxation towards a nearby metastable state using conjugate gradients [40], as well as for the computation of migration energies with the nudged elastic band method (NEB) [41,42]. Such potentials, henceforth referred to as lattice-free potentials, imply the knowledge of the atomic coordinates in any equilibrium and nonequilibrium configuration, which is unnecessary and incompatible with atomistic models formulated in a rigid-lattice framework, such as Monte Carlo methods. However, in order to include the effect of atomic relaxations, it is convenient to develop specific types of potentials, henceforth referred to as rigid-lattice

potentials. They are able to compute the total energy of a given atomic configuration after relaxation (i.e., with no residual forces), while receiving as input its rigid-lattice description. Atomic forces need not to be estimated because they are inherently assumed to have vanished.

In both rigid-lattice and lattice-free cases, and consistently with the prerequisites for high-dimensional potentials, the total energy is decomposed as proposed by Behler and Parrinello [29] as a summation of contributions from each individual atom:

$$E_{\mathrm{ANN}}^{(\mathrm{Tot})} = \sum_{a=1}^{N} E^{(a)}. \tag{1}$$

Here, superscript (a) refers to a particular atom within the N constituting the studied configuration, and $E^{(a)}$ are the energies associated to each of them. These individual energies can be regarded as functions of the local atomic densities:

$$E^{(a)} = f(\rho^{(a)}). \tag{2}$$

Here, $\rho^{(a)}$ stands for the local density at the position occupied by atom (a). Function f is, similarly to the approach of Behler *et al.*, implemented using a classical form of ANN designated in the literature as a "multilayer perceptron" [43]. It must thus be specifically defined for every chemical species involved, e.g.,

$$E_{\mathrm{ANN}}^{(\mathrm{Tot})} = \sum_{a=1}^{N} E_{\mathrm{ANN}}^{(X(a))}(\rho^{(a)}). \tag{3}$$

Here, $X(a)$ denotes the chemical species for atom (a), i.e., $X(a) = \mathrm{Fe}, \mathrm{Cu}, \mathrm{Cr}, \ldots$. Functions $E_{\mathrm{ANN}}^{(X(a))}$ are henceforth called atomic energy functions (AEFs), providing an estimation of the energy assigned to every atom of the corresponding chemical species. Subscript ANN refers to the fact that each AEF is implemented by an individual ANN.

B. Description of local atomic densities as ANN input variables

We exploit similar ideas to those proposed by Bartók *et al.* [44] to expand the local atomic density into symmetry functions using series expansion in spherical harmonics:

$$\rho^{(a)}(r,\theta,\varphi) = \sum_{n=1}^{\infty}\sum_{l=0}^{\infty}\sum_{m=-l}^{l} C_{nlm}^{(a)} R_n(r) Y_{lm}(\theta,\varphi). \tag{4}$$

Here, (r,θ,φ) are spherical coordinates with the origin set at the position where atom (a) is sitting, Y_{lm} are the Laplace spherical harmonics functions, and $C_{nlm}^{(a)}$ are coefficients determined below. The terms R_n are series of any radial functions. Here we choose

$$R_n(r) = \sin\left(\frac{n\pi r}{R_{\mathrm{c}}}\right) f_R(r), \tag{5}$$

where r is the distance from the origin, n is a positive integer, and R_{c} is a given cutoff. The radial shaping factor f_R is defined as

$$f_R(r) = \left[\frac{R_{\mathrm{c}}}{r}\right]\left[0.5\left\{1 + \tanh\left(-\alpha\frac{r}{R_{\mathrm{c}}} + \beta\right)\right\}\right]. \tag{6}$$

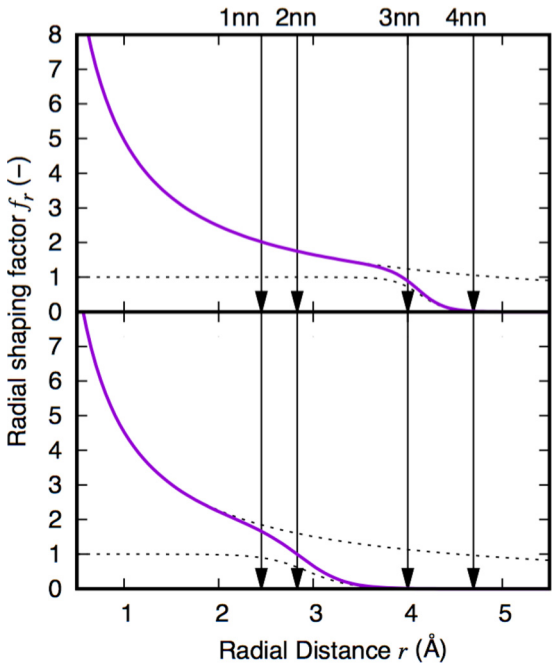

FIG. 1. Radial shaping factors used in this work, i.e., bcc Fe-based alloys with $a_0 = 2.831$ Å. Dashed curves show the two terms in Eq. (6), and vertical arrows the distances associated with shells of nearest neighbors in bcc. Top: Cutting interaction between the 3nn and the 4nn distances: $R_{\mathrm{c}} = 1.75a_0 = 4.954$ Å, $\alpha = 18$, and $\beta = 15$. Bottom: Cutting interaction between the 2nn and the 3nn distances: $R_{\mathrm{c}} = 1.6a_0 = 4.530$ Å, $\alpha = 10$, and $\beta = 6.5$.

Here, square brackets separate the contribution from two different terms, as illustrated in Fig. 1. The first one introduces a strong repulsion for short interatomic distances in the form of a Coulomb potential (energy $\propto 1/r$; force $\propto 1/r^2$), whereas the second one constrains the radial interaction to fade away near the prescribed cutoff R_{c}; α and β are calibration parameters chosen according to the range of distances where the interaction should be damped.

In the above equations, subscripts n, l, and m are integers defining the complexity of the expansion. The coefficients $C_{nlm}^{(a)}$ are calculated using

$$C_{nlm}^{(a)} = \iiint_{r,\theta,\varphi} \rho^{(a)} R_n(r) Y_{lm}(\theta,\varphi) r^2 \sin(\theta) d\theta d\varphi dr. \tag{7}$$

Some analytical expression for the atomic density must thus be provided, e.g., a collection of Dirac deltas sitting on the nearby atoms. We thus derive

$$C_{nlm}^{(a)} = \frac{1}{N_{\mathrm{RC}}^{(a)}} \sum_{i=1}^{N_{\mathrm{RC}}^{(a)}} R_n(r_i) Y_{lm}(\theta_i,\varphi_i). \tag{8}$$

Here, $N_{\mathrm{RC}}^{(a)}$ is the number of atoms found within R_{c} from atom (a). Invariance with rigid rotations is achieved by performing the summation in Eq. (8) over the m parameter:

$$Q_{nl}^{(a)} \triangleq \sum_{m=-l}^{l} \left| C_{nlm}^{(a)} \right|^2. \tag{9}$$

Parameters n and l may theoretically vary from 0 to any integer number as large as necessary for the desired complexity of the

expansion. In practice, a maximum value for both (denoted respectively as N_{Max} and L_{Max}) is chosen and a full vector is thereby defined:

$$\bar{Q}^{(a)} \triangleq \left[Q_{nl}^{(a)}\right] \tag{10}$$

with $1 \leqslant n \leqslant N_{\mathrm{Max}}$ and $0 \leqslant l \leqslant L_{\mathrm{Max}}$. Information about the chemical species is included with the approach taken by Behler *et al.* [33]. Considering the example of a binary FeX alloy, three distinct $\bar{Q}$ vectors are combined, each including the contribution from chemical sub-ensembles in the neighboring atoms, i.e.,

$$\bar{Q}^{(a)} \triangleq \left[Q_{\mathrm{FeFe}}^{(a)} Q_{\mathrm{FeX}}^{(a)} Q_{\mathrm{XX}}^{(a)}\right]. \tag{11}$$

Here, $Q_{\mathrm{Fe}}^{(a)}$, $Q_{\mathrm{X}}^{(a)}$, and $Q_{\mathrm{FeX}}^{(a)}$ are identical as defined in Eq. (9), but only consider either Fe atoms, X atoms, or both, respectively. Given N_{Max} and L_{Max}, the number N_Q of symmetry functions (corresponding to the ANN input variables) is thus given by

$$N_{\mathrm{Q}} = 3N_{\mathrm{Max}}(L_{\mathrm{Max}} + 1). \tag{12}$$

C. Potential fitting

Consistently with the usual practice, ANN training requires regularization, i.e., a mean to either monitor the prediction capabilities for never seen cases. We use an "early stopping" approach [43], meaning that a part of the available database is reserved to define a reference set aimed at following the evolution through fitting of the average error committed for new cases. We typically reserve 25% of the available data for that purpose, while the remaining 75% are used to perform the fit, minimizing the following objective function:

$$f(\bar{W}) = \sum_{t=1}^{T} \left[E_{\mathrm{ANN}}^{(t)}(\bar{W}) - E_{\mathrm{DFT}}^{(t)}\right]^2. \tag{13}$$

Here, superscript (t) refers to each of the cases in the training set T, and superscript (a) refers to each atom out of $N^{(t)}$ in case t. The variables for the training problem are the entries of vector $\bar{W}$. The latter represents the combined vector of all degrees of freedom in all the AEFs, i.e., the numerical coefficients found in the ANN internal structures whose exact numerical value must be determined. They are commonly called "synapses" in the literature [43]. The vector is written, in case of binary Fe-X alloys, as

$$\bar{W} \triangleq [\bar{W}_{\mathrm{Fe}} \bar{W}_{\mathrm{X}}]. \tag{14}$$

Minimizing function $f(\bar{W})$ is a nonlinear optimization problem, unbounded and unconstrained in its input space. We use a Levenberg-Marquardt (LM) algorithm, as already used and detailed in previous works [24–26].

D. Reference databases of configurations

NNP fitting requires as primer input a database of representative atomic configurations for the targeted purpose. The main concern is the ability to handle new kinds of configurations that may be encountered during the simulations. In rigid-lattice MC models, the atomic structure remains in principle nearly identical through AKMC or MMC simulations (unless lattice defects form large clusters). Similarly to discussions

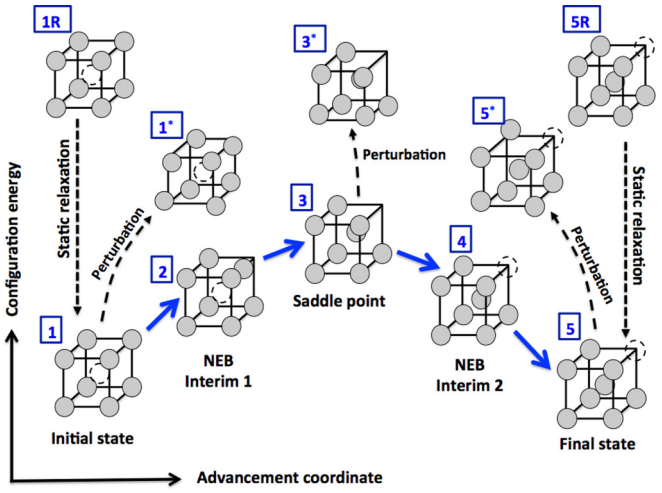

FIG. 2. Atomic configurations extracted from DFT-NEB calculations in this work. Each cubic box with 8 atoms (gray circles) pictorially depicts a DFT calculation supercell ($5a_0 \times 5a_0 \times 5a_0$) for the case of vacancy migration (dashed circle).

in Refs. [24,25,36], the major concern is thus the occurrence of new local chemical configurations around migrating point defects. A valid strategy to build a NNP training database is thus to gather atomic configurations while performing NEB calculations, for adequately chosen examples of point-defect migration events. Typically, the calculation proceeds with the construction of a chain of transition states from an initial to a final configuration, as depicted in Fig. 2. The explored configurations are here categorized in different sets:

Set 1. End states associated with the point-defect migration events, denoted as state 1 and state 5 in Fig. 2.

Set 2. Saddle-point configurations obtained with NEB (state 3 in Fig. 2).

Set 3. States selected among the many intermediate calculations performed, including the intermediate NEB images (2 and 4 in Fig. 2), and the relaxation steps from the rigid-lattice description of the end states (states 1R and 5R in Fig. 2).

Set 1 alone is fully exploitable for designing NNPs in a rigid-lattice framework, whereas lattice-free potentials require sets 2 and 3. To our experience, however, using these sets of training samples only is insufficient to produce fully satisfactory NNPs. This can be explained by the intrinsic high degree of correlation that characterizes such a database (all configurations describe, from an atomic structure point of view, nearly identical events of point-defect migration). Additionally, the focus on energy-matching in our fitting procedure purposely favors very accurate NNPs for describing the energetics of metastable configurations (given their atomic coordinates), but may not find these configurations during a relaxation process. Including an explicit force-matching criterion in Eq. (13) can improve the NNP quality in that respect. In the framework of MC modeling, the main interest for including this component is to ensure that residual forces vanish for atomic configurations close to metastable states. From this point of view, the key information to transfer from DFT to the NNP is that the total energy should always increase when slightly deviating from a metastable state. To achieve that goal in the simplest way, and specifically keep

a full energy-matching strategy, we included a fourth set in the training database. The latter features configurations where the atoms are slightly displaced in random directions from the equilibrium positions describing a metastable state.

Set 4. Configurations randomly departed with small atomic displacements from state 1, state 3, and state 5, respectively denoted as state 1*, state 3*, and state 5* in Fig. 2. An individual displacement vector is applied to all atoms, with an effective magnitude randomly chosen between 0 and a maximum value henceforth denoted as D^*_{Max}.

Obtaining these configurations entails a very small additional CPU load compared to the rather sizable set of NEB calculations, because the total energy is obtained with a static one-step DFT energy calculation.

III. APPLICATIONS TO FeCu AND FeCr ALLOYS

The binary FeCu and FeCr alloys are illustrative cases for the application of the methodologies exposed in Sec. II. Ample experience has been gathered in modeling thermal annealing processes in these systems during the last decades, as well as irradiation experiments, among others with our AKMC methodology based on IAPs [24,25]. The added value of referring to *ab initio* methods as a source of physics can thus be thoroughly evaluated.

The section is organized as follows. In Sec. III A, we start by describing the databases of DFT atomic configurations used in this work. Then, in Sec. III B, rigid-lattice potentials are fitted for both alloys, and MMC simulations are performed to analyze the predicted phase diagrams, thereby performing a preliminary thermodynamic assessment. Kinetics is included later in Sec. III C, where thermal-annealing experiments in a FeCr alloy are simulated by means of AKMC. The rigid-lattice potential is used to evaluate the equilibrium energies, while another specifically trained ANN is used for estimating the activation energies associated with vacancy migration events. Finally, lattice-free potentials are fitted in Sec. III D for both systems. The case of FeCr is particularly significant, because atomic configurations including both vacancies and self-interstitial atoms (SIAs) are successfully handled within the same NNP. The latter is then used to extend the database of single-SIA migration energies, which allows for a considerable improvement of the accuracy of the kinetic model.

A. Databases of DFT data used in this work

The databases of DFT data used in this work are obtained from static relaxations and NEB calculations performed with the Vienna *ab initio* simulation package (VASP) [45–47]. The calculations are made on a plane-wave basis, with the pseudopotentials derived within the projector-augmented wave (PAW) method [48,49]. The Perdew-Burke-Ernzerhof (PBE) parametrization [50] of the generalized-gradient approximation (GGA) is employed to represent the exchange-correlation function. All calculations are spin polarized, with a Vosko-Wilk-Nusair (VWN) spin interpolation of the correlation potential [51], and the Brillouin zone is sampled within a Monkhorst-Pack scheme. The standard full-core potentials available in the VASP library are employed for Fe, Cu, and Cr atoms, with a plane-wave cutoff energy set to 300 eV. The simulation volume consists of $5 \times 5 \times 5$ supercells in a body-centered cubic structure (i.e., 250 atomic sites), with full periodic boundary conditions. Both the end-state relaxations and the NEB calculations are at constant volume, where the cell shape is restrained but atomic relaxations are allowed. The total ionic relaxation energies are converged with a tolerance of 1 meV, whereas the NEB calculations, performed with 3 images and the climbing-image algorithm [41,42], are converged when the residual force on each atom is below 20 meV/Å. For the end-state relaxations, a $3 \times 3 \times 3$ k-point grid is employed to perform numerical integration in the reciprocal space. On the other hand, for improved efficiency, the NEB calculations are performed using a reduced k-point grid ($2 \times 2 \times 2$), and the actual migration energy path is then recalculated by doing a one-step energy calculation with the full $3 \times 3 \times 3$ k-point mesh, not allowing for any ionic relaxation of the images obtained with the reduced grid. This accelerated procedure assumes that the atomic configurations of the NEB images are not greatly affected by the choice of the k-point mesh; however, the associated energy is undoubtedly k-point dependent and is therefore recalculated with one quick additional ionic step. It was checked for a few sample cases that the difference between this accelerated procedure and a full k-point NEB calculation is always smaller than 1 meV. It is worth noticing that because of this procedure the residual forces on each atom in the intermediate images might be higher than the minimum achievable by the optimization algorithm. Such residual forces are anyway never greater than 30 meV/Å. Finally, the energy calculations for configurations slightly departed from the metastable states are performed in a single ionic step, with the same setup parameters and a full $3 \times 3 \times 3$ k-point mesh.

Data for the FeCu alloy is taken from Ref. [36]: it is a collection of 2000 vacancy migration energies in a changing local atomic environment sampled in representative configurations of the early coherent stages of Cu precipitation. Next, another group of 2000 cases of single-vacancy migration in concentrated FeCr alloys has been generated, by following a selection procedure analogous to that described in Ref. [24]. Solute Cr atoms were allocated in random solid solution, with varying concentrations between 2% and 50%. Last, a third group of 5600 cases of single-SIA migration has been calculated in FeCr alloys of similar composition. Following our work in Ref. [52], three kinds of migration events were considered: from a dumbbell ⟨110⟩ orientation, the SIA migrates towards a first-nearest-neighbor (1nn) position and performs a pure translation or a 60° rotation-translation to a symmetrically equivalent ⟨110⟩ orientation.

The amount of atomic configurations collected in each of the above-listed sets is summarized in Table I. Furthermore, a small set of additional configurations was included to characterize fundamental Fe properties, such as perfect supercells with varying lattice parameters around the DFT equilibrium value ($a_0 = 2.831$ Å), or a detailed NEB description of single-vacancy migration in pure Fe. Finally, it is worth mentioning that the target for energy fitting has been systematically converted, for convenience, into a formation energy of the supercell assumed to be, without loss of generality,

$$E^* = E^{(t)}_{\mathrm{DFT}} - [-8.2N_{\mathrm{Fe}} - 3.6N_{\mathrm{Cu}} - 9.5N_{\mathrm{Cr}}]. \qquad (15)$$

TABLE I. Summarizing description of the DFT database of atomic configurations used in this work.

	Number of NEB calculations	CPU time (h)	Number in Set 1	Number in Set 2	Number in Set 3	Number in Set 4
FeCu, vacancy	2000	9 million	4000	2000	12000	4768 $D^*_{\text{Max}} = 0.1a_0; 0.07a_0$
FeCr, vacancy	2000	10 million	4000	2000	12000	6000 $D^*_{\text{Max}} = 0.07a_0; 0.05a_0$
FeCr, SIA	5600	30 million	11200	5300	33000	24000 $D^*_{\text{Max}} = 0.05a_0; 0.015a_0$

The coefficients above, given in units of eV, are close to the cohesive energy per atom of each pure element obtained with the same DFT parameters. This somewhat arbitrary normalization does not affect the NNP accuracy, but is more suitable for ANN training because the energy variations among configurations are largely reduced.

In Fig. 3, we compare the predicted values for the end-state energy differences and the migration energies with the predictions from the EAM potentials used in Refs. [24,25]. In the case of the FeCu system, the EAM potential (described in Ref. [53]) appears to perform predictions that are well correlated with the DFT values. The prediction of the end-state energy difference, which governs thermodynamics, is more satisfactory than that of the migration energies. It was thoroughly described in Ref. [36] that an AKMC model fed with the DFT-based migration energies significantly improved the prediction of kinetics for the precipitation of Cu in Fe. Concerning the FeCr system, the predictions from the EAM potential (described in Ref. [54]) are clearly uncorrelated with DFT. Even though the implications on the quality of AKMC predictions cannot be anticipated, Fig. 3 proves that empirical interatomic potentials and DFT provide very different descriptions of the physical properties of this alloy. The improvements in the simulation of microstructure evolution brought by our model are evaluated later in Sec. III C.

B. Thermodynamic modeling with rigid-lattice potentials

As presented in Sec. II A, rigid-lattice potentials are convenient tools for following the evolution of the total energy associated with the studied alloy during MMC or AKMC simulations where static relaxation is not formally applied. The atomic system under investigation is constantly described in a rigid-lattice framework, and so are the input variables to the ANN potentials. Rigid-lattice potentials for both the FeCu and the FeCr alloys were obtained. Their prediction accuracy is very satisfactory, as shown in Fig. 4 and summarized in Table II. The FeCr potential was fitted including all available cases, i.e., those involving a single vacancy and also those involving a single SIA.

Figure 5 shows the phase diagrams of both systems, as obtained with the aforementioned NNPs by means of MMC

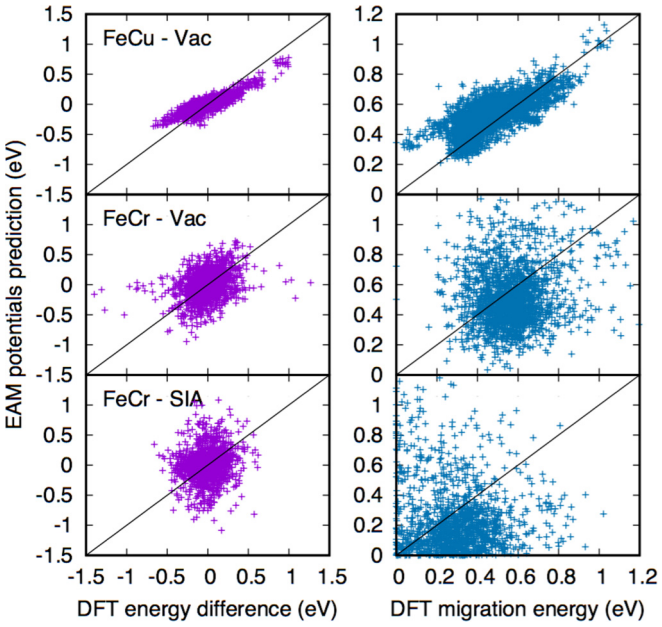

FIG. 3. Comparison of the (left) end-state energy differences and (right) migration energies found by NEB using DFT or the EAM potentials.

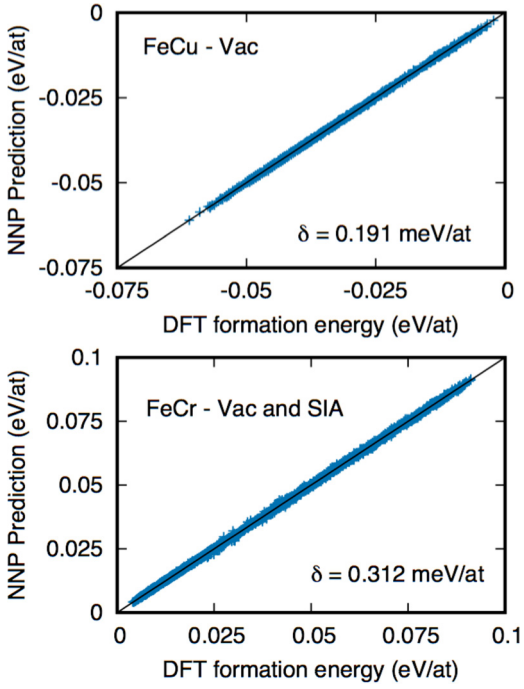

FIG. 4. Accuracy of prediction by the rigid-lattice NNPs of the supercell formation energy [defined in Eq. (15)]. δ is the mean absolute error of prediction, reported in Table II.

TABLE II. Summary of ANN potentials fitted in this work: architectures and residual errors of predictions measured on the respective reference sets. H stands for the number of hidden nodes in the ANN (in one single hidden layer), and W stands for the number of adjusting parameters (synapses). R^2 is Pearson's correlation coefficient.

	ANN description		Residual mean absolute errors of prediction			
	Input variables	Architecture	Configuration energies	Atomic forces	ΔE	Migration energies
FeCu rigid lattice	$R_c = 1.6a_0$ $N_{Max} = 3$ $L_{Max} = 10$ $N_Q = 99$	$H = 3$ $W = 304$	0.191 meV/atom $R^2 = 0.99$	Non-applicable	42.4 meV $R^2 = 0.98$	Non-applicable
FeCr rigid lattice	$R_c = 1.75a_0$ $N_{Max} = 5$ $L_{Max} = 7$ $N_Q = 120$	$H = 3$ $W = 367$	0.312 meV/atom $R^2 = 1.0$	Non-applicable	68.5 meV $R^2 = 0.88$	Non-applicable
FeCu lattice-free	$R_c = 1.6a_0$ $N_{Max} = 5$ $L_{Max} = 10$ $N_Q = 165$	$H = 3$ $W = 502$	0.171 meV/atom $R^2 = 1.0$	46.7 meV/Å $R^2 = 1.0$	26.4 meV $R^2 = 0.99$	31.2 meV $R^2 = 0.98$
FeCr lattice-free	$R_c = 1.75a_0$ $N_{Max} = 5$ $L_{Max} = 10$ $N_Q = 165$	$H = 3$ $W = 502$	Single vacancy cases:			
			0.345 meV/atom $R^2 = 1.0$	79.3 meV/Å $R^2 = 0.96$	48.8 meV $R^2 = 0.90$	59.9 meV $R^2 = 0.85$
			Single SIA cases:			
			0.302 meV/atom $R^2 = 1.0$	71.2 meV/Å $R^2 = 0.94$	54.1 meV $R^2 = 0.92$	60.2 meV $R^2 = 0.89$

simulations in the transmutation ensemble. The methodology here followed is fully analogous to that described in Ref. [55]. The phase diagram of the FeCr system is remarkably consistent with the experimental data revision by Bonny *et al.* [56]: no Cr clustering is expected to occur at any temperature, unless the Cr concentration exceeds about 9 at.%. As is discussed in more detail in Ref. [57], the expected discrepancy at larger concentrations can be attributed to the lack of magnetic and vibrational entropy in the rigid-lattice MMC model.

On the other hand, the solubility limit in the FeCu alloy is underestimated with respect to the previous EAM-based work [58] as well as to the theoretical estimates in the coherent bcc Fe/bcc Cu system, obtained with the ATAT method [53]. However, this discrepancy is consistent with the excessive Cu precipitation observed in Ref. [36], which can be ascribed to the faulty DFT prediction of the Cu solution energy in Fe by the PBE functionals [17,59].

C. Kinetic modeling with AKMC

As a test application, we present the simulation of a thermal-annealing experiment in a Fe 20 at.% Cr alloy at 500 °C. The simulation starts from a random solid solution constituted by a bcc Fe matrix with 20% Cr, and a single vacancy. We are inspired by Kang and Weinberg [60] to split the associated migration barrier into two separate contributions as follows:

$$E^{(mig)} = \frac{\Delta E^{(Tot)}_{ANN}}{2} + E^{(act)}_{ANN}. \quad (16)$$

Here, $\Delta E^{(Tot)}_{ANN}$ is the contribution from the difference in energy between the end states associated with each vacancy jump. Subscript ANN marks that the ΔE is evaluated with the rigid-lattice NNP obtained in Sec. III B. The remaining activation energy $E^{(Tot)}_{ANN}$ is then predicted by an independent ANN, trained on the basis of the end-state relaxation (set 1) and the saddle-point (set 2) databases. The methodology followed to design this ANN is thoroughly described in Ref. [24]. The accuracy of prediction achieved with the obtained ANN is illustrated in Fig. 6.

The obtained results from the AKMC simulation are illustrated in Fig. 7. The evolution in time of the Cr cluster density and average radius is compared with the experimental observations by atom probe tomography (APT) by Novy [61,62] and Jacquet [63], as well as those by small-angle neutron scattering (SANS) by Bley [64]. The AKMC simulation time is rescaled in order to compensate for the higher vacancy concentration in the simulation box ($40a_0 \times 40a_0 \times 40a_0$) compared to the real thermal-equilibrium value. This was performed assuming that the vacancy formation energy in the alloy is, on average, 1.85 eV. Our results previously obtained in Ref. [24] with an IAP are also shown for comparison. It is worth noting that the cluster populations obtained in Ref. [24] and in this work are analyzed with a new algorithm that attempts to reproduce more realistically the stochastic nature of the APT experimental technique, as is described in the Appendix. The results shown in Fig. 7 highlight that the present DFT-based model deviates significantly from our previous IAP-based predictions: the average cluster radius is smaller, while the cluster density remains globally in agreement. Both series seem in fact to lie at the edges of the range of experimental values, and both could thereby be judged as equally acceptable. However, our present model shows full consistency with the series of Novy and Bley, for what concerns both the average radius and the cluster density. Furthermore, Novy *et al.* [61,62]

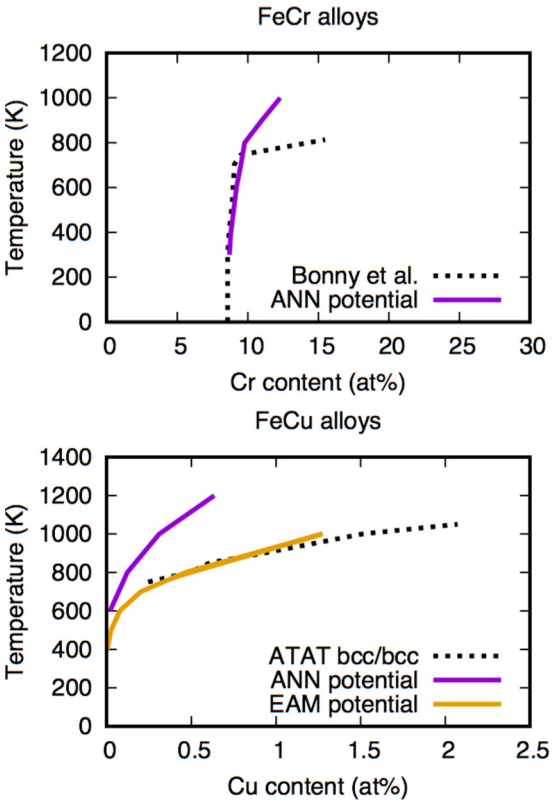

FIG. 5. Phase diagrams predicted with the rigid-lattice NNPs obtained in this work. Bottom: FeCu case. The dashed line shows a calculation with the ATAT method for the bcc/bcc coherent phase in Ref. [53]. The prediction with the EAM potential is taken from Ref. [58]. Top: FeCr case. The dashed line is a review of experimental evidence by Bonny *et al.* in Ref. [56].

criticized the validity of the APT measurements by Jacquet [63], and argued for a more likely consistency of their results with the SANS measurements by Bley *et al.* [64]. As of today, this statement is generally well accepted, and Jacquet's data are normally discarded [65]. Our current DFT model is therefore in better agreement with the experimental evidence than the previous IAP model. Finally, our results are also in excellent agreement with the AKMC simulations by Martinez *et al.* [66], which were supported by a DFT-based pair-interaction energy model that explicitly accounted for some entropic contributions (namely to the mixing and vacancy activation energies).

D. Lattice-free potentials fitting and application

In this section, lattice-free potentials are designed for FeCu and FeCr alloys. In contrast with the rigid-lattice application in Secs. III B and III C, all sets of data described in Sec. II D are included in the fit. The obtained results are illustrated in Fig. 8 and summarized in Table II. The predictions of the total energies are in excellent agreement with DFT. Additionally, we observe the following: (a) Predictions of atomic forces appear to be highly correlated with the DFT forces, even though this information was not explicitly included in the fit. This shows that our energy-matching strategy, with the inclusion of small random perturbations, is able to transfer

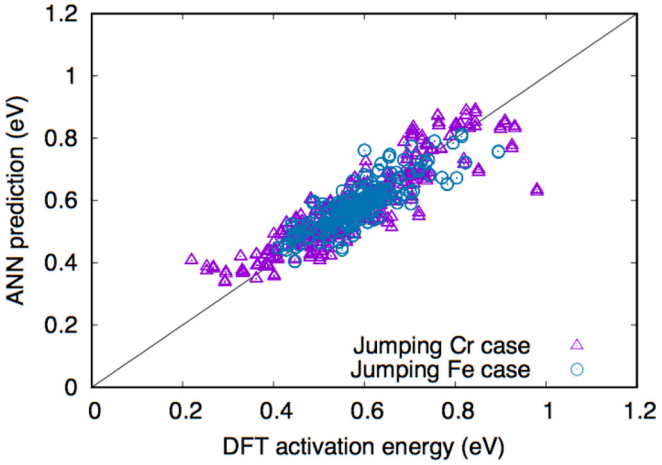

FIG. 6. ANN quality of prediction for the activation energy associated with vacancy migration in FeCr alloys. Only points from the reference set are shown. The residual mean absolute error of prediction is 48.3 meV ($R^2 = 0.90$) for the jumping Fe case, and 32.9 meV ($R^2 = 0.86$) for the jumping Cr case.

information about the kinetics of the system to the potential, while being originally mainly focused on static properties. (b) Globally, as summarized in Table II, all NNPs obtained here are relatively light (i.e., containing fewer free parameters, or "synapses") compared to those reported for other applications (see, e.g., Ref. [30]). Also, the residual mean absolute error on the total-energy prediction is significantly under 1 meV/atom, which is comparable to the best prediction accuracies achieved in other works [38]. This is likely due to the purpose-specific target of our application, i.e., the focus on point-defect-driven microstructure evolution.

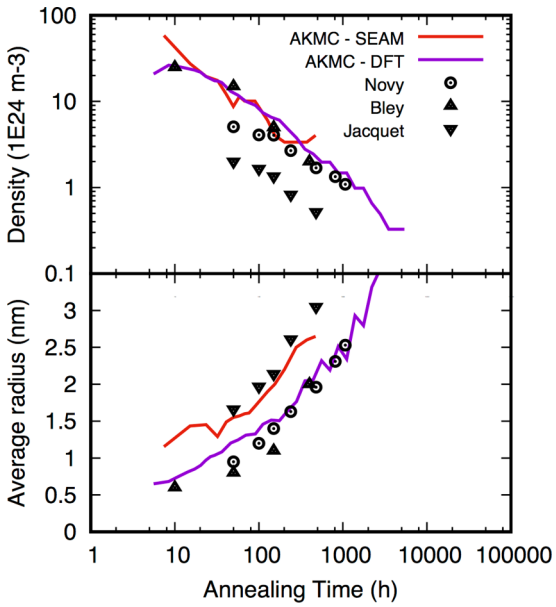

FIG. 7. Prediction with AKMC of a thermal annealing experiment on an Fe 20% Cr alloy at 500 °C. Both results obtained in this work (labeled AKMC-DFT) and in Ref. [24] (labeled AKMC-SEAM) are shown. APT experimental data are taken from Novy [61,62], Jacquet [63], and Bley [64].

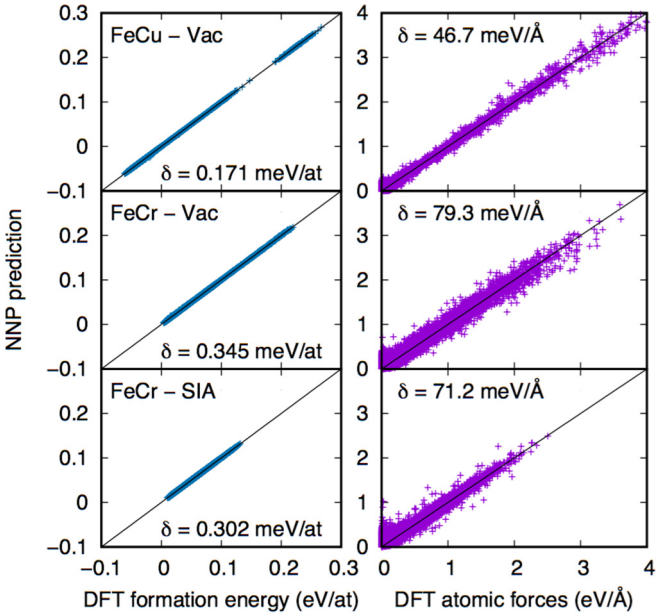

FIG. 8. Accuracy of prediction achieved by the lattice-free NNPs designed for the FeCu and FeCr systems. Reference values are taken from the databases of configurations described in Sec. II D, and formation energies are defined in Eq. (15). The figures for the latter are split into the vacancy migration events and the SIA migration events. δ is the mean absolute error of prediction, reported in Table II.

Finally, we test the predictive capabilities of computing point-defect migration energies using no previous knowledge of the metastable states involved in the transitions. For that purpose, we used the obtained lattice-free NNPs to perform NEB calculations and recompute the DFT migration barriers originally included in the training database (see Table I). Prior to the NEB calculation, the end states were systematically departed from the ideal rigid-lattice positions, and a full static

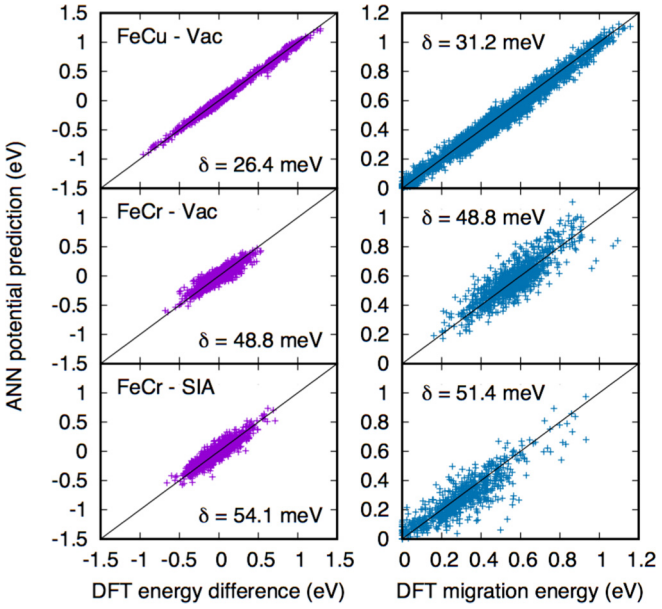

FIG. 9. Comparison of the end-state energy differences (left) and NEB migration energies (right), found using DFT or the NNPs. δ is the mean absolute error of prediction, reported in Table II.

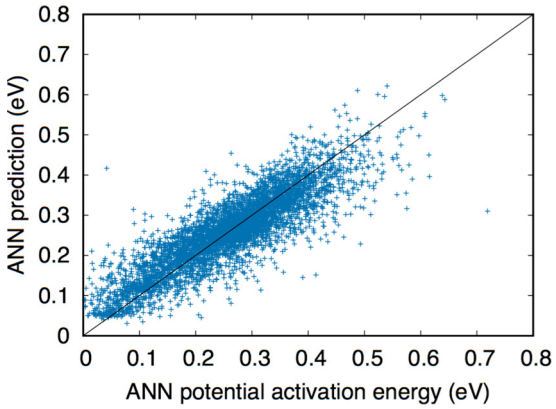

FIG. 10. ANN quality of prediction for the migration energy associated with single-SIA migration in FeCr alloys. Target values were obtained with the NNP. The residual mean absolute error of prediction is 39.1 meV ($R^2 = 0.89$).

relaxation was performed. Comparison between the predicted energy differences and migration energies is illustrated in Fig. 9, and summarized in Table II. Clearly, we see that our NNP's succeeded in mimicking the relevant aspects of DFT for our modeling, because all crucial properties of the studied migration events (i.e., the energy difference between end states and the migration energy) are faithfully reproduced on average. Errors on some individual cases may be regarded as relatively large, but this is of no concern, because the objective of these potentials is to predict the average behavior of the alloy, which depends on a large number of migration events. We can thus fairly confidently state that these potentials may be used to evaluate new cases in order to enhance the capabilities of producing training samples by DFT, in terms of larger amounts of cases within small computational efforts, as well as larger simulation cells. As a matter of fact, the originally calculated 5600 cases of single-SIA migration events in FeCr alloys were not sufficient to achieve a kinetic model, with a performance as satisfactory as the one shown in Fig. 6 for the single-vacancy case. Thanks to the lattice-free NNP, however, we were able to extend this database to 30 000 new cases with a very limited CPU cost, achieving a much more accurate model, as illustrated in Fig. 10.

IV. CONCLUDING AND SUMMARIZING REMARKS

In this work, we have taken a few steps towards the objective of relying exclusively on large databases of *ab initio* properties to reproduce the thermodynamic and kinetic properties of an alloy during atomistic Monte Carlo (AMC) simulations. Our strategy relies on high-dimensional neural-network potentials (NNP) fitted on point-defect migration energies evaluated with density functional theory (DFT), thus targeting the specific needs of rigid-lattice models. With respect to traditional atomistic MC approaches, neural networks allow for an efficient exploitation of massive amounts of DFT calculations, thanks to the high-dimensional mathematical structure they provide. This can be regarded as the most accurate way to transfer physical information from the *ab initio* to the Monte Carlo scale. With respect to our previous work [36] where

DFT-trained neural networks were used to predict vacancy migration barriers in kinetic Monte Carlo simulations, the NNPs developed here ensure a more accurate parametrization, as they predict not only the energy barrier of a defect migration event, but also the energy associated with metastable and saddle-point states. This opens the possibility to perform metropolis Monte Carlo simulations and therefore allows for a preliminary thermodynamic assessment of the system, which is not possible if only migration barriers are predicted. Moreover, splitting the prediction of the end-state energies from that of the saddle-point energies with independent ANNs enables the user to choose independent strategies or methods to address thermodynamic and kinetic properties separately, providing the necessary leverage to correct issues such as the incorrect solubility limit of Cu in Fe [36]. In addition, the lattice-free potentials allow for an extension of the DFT capabilities: it has been shown how they can be used as numerical tools to mimic the DFT framework and efficiently perform large amounts of NEB calculations. This leads to the creation of much richer migration-barrier databases that are necessary for treating more complex cases, such as SIA migration or multicomponent alloys. Lastly, the lattice-free potentials can also potentially solve the DFT cell-size problem encountered in the previous work. For instance, obtaining data from larger simulation cells would allow for cases of defect migration next to large solute clusters to be included in the training databases.

A systematic and efficient introduction of DFT databases in the parametrization of AMC models in place of traditional interatomic potentials is highly desirable, as it would greatly simplify the application to complex alloys and would ensure a level of physical accuracy as close as possible to that provided by first-principles methods. For instance, the application here presented to FeCr thermal-annealing simulations has shown that the NNP-based parametrization has greatly improved the match with the experimental data with respect to the previous EAM results. In conclusion, this work gives a substantial contribution to the ongoing effort of employing high-throughput computational techniques in the modeling of microstructure evolution, which can support the linking of first-principles calculations with higher-scale methods. Ensuring the best possible transfer of physics across modeling scales is indeed necessary to achieve fully reliable multiscale models that can aid understanding and predicting materials behavior in a wide range of applications and conditions.

ACKNOWLEDGMENTS

This work was partly supported by the H2020 European project SOTERIA (No. 661913) and the FP7-Euratom-Fission European project MATISSE (No. 661913) and Vattenfall AB. It contributes to the Joint Programme on Nuclear Materials of the European Energy Research Alliance. Private communication within the European FP7/NUGENIA-PLUS APLUS Grant No. 604965 is also acknowledged, for finding a common agreement on how the results of our AKMC simulations could be analyzed with the eyes of the atom probe tomography. N.C. acknowledges partial funding by the Argentine PIP-CONICET 804/10 project at the early premises of this work. The DFT calculations, representing about 50 million CPU core hours, were performed on EDF HPC resources Athos and Porthos supercomputers (respectively 18144 Intel Xeon E5-2697v2 12C 2.7 GHz cores and 16300 Intel Xeon E5-2697v3 14C 2.6 GHz cores).

APPENDIX: APT-LIKE CLUSTER ANALYSIS

One way to assess the results obtained by atomistic Monte Carlo (MC) models is to compare them with experimental observations by atom probe tomography (APT). However, it is delicate to perform in practice. On the one hand, the atomic system is described with full details in the MC model: any defects in the microstructure, such as clusters of solute atoms (even very small ones), are unequivocally identifiable. On the other hand, even if APT allows for a very accurate atomic-level characterization of real materials, it cannot achieve an equally perfect description: about half of the atoms are unavoidably undetected, and the spatial coordinates of the other atoms are significantly distorted. These effects should be taken into account while analyzing the results of our atomistic kinetic Monte Carlo (AKMC) model, in order to realistically reproduce the nonperfect efficiency of detection of solute clusters by APT.

Inspired by collaborative discussions with colleagues [65,67], we established an algorithm to mimic the APT while analyzing our AKMC results. It can be briefly summarized as follows. (a) In order to account for the APT detection accuracy, 60% of the atoms in the simulation cell are chosen at random and discarded. (b) Since large distortions in the atomic coordinates are inherently induced by the measurement, especially in the plane perpendicular to the sample main axis (very thin needle), the remaining atoms in the simulation cell are randomly displaced along that plane. The displacement magnitude follows a Gaussian distribution with a full width at half maximum (FWHM) as large as 0.75 nm, while a smaller value (0.1 nm) is applied in the direction of the sample axis. (c) Finally, clusters are identified by searching for groups of neighboring atoms, with a cutoff distance of $1.75a_0 = 4.954$ Å. The cluster radii are calculated with the Guinier formula. In summary, this procedure mimics the dissolution of small clusters of solute atoms at the beginning of the APT measurement, as well as the average increase of cluster size due to the APT-induced local displacements.

[1] A. B. Bortz, M. H. Kalos, and J. L. Lebowitz, J. Comput. Phys. **17**, 10 (1975).

[2] Y. Le Bouar and F. Soisson, Phys. Rev. B **65**, 094103 (2002).

[3] P. Krasnochtchekov, R. S. Averback, and P. Bellon, Phys. Rev. B **75**, 144107 (2007).

[4] G. Bonny, D. Terentyev, L. Malerba, and D. Van Neck, Phys. Rev. B **79**, 104207 (2009).

[5] C.-C. Fu, J. D. Torre, F. Willaime, J.-L. Bocquet, and A. Barbu, Nat. Mater. **4**, 68 (2005).
[6] Y. Fan, A. Kushima, S. Yip, and B. Yildiz, Phys. Rev. Lett. **106**, 125501 (2011).
[7] M. Chiapetto, L. Malerba, and C. Becquart, J. Nucl. Mater. **462**, 91 (2015), and references therein.
[8] C. L. Liu, G. R. Odette, B. D. Wirth, and G. E. Lucas, Mater. Sci. Eng. A **238**, 202 (1997).
[9] F. Soisson, C. S. Becquart, N. Castin, C. Domain, L. Malerba, and E. Vincent, J. Nucl. Mater. **406**, 55 (2010).
[10] E. Vincent, C. S. Becquart, and C. Domain, J. Nucl. Mater. **382**, 154 (2008).
[11] R. Ngayam-Happy, C. Becquart, C. Domain, and L. Malerba, J. Nucl. Mater. **426**, 198 (2012).
[12] Y. Zhang, P. Chakraborty, and S. B. Biner, Modeling of Late Blooming Phases and Precipitation Kinetics in Aging Reactor Pressure Vessel (RPV) Steels, Tech. Rep., Idaho National Laboratory (INL), 2013.
[13] W. M. Young and E. W. Elcock, Proc. Phys. Soc. London **89**, 735 (1966).
[14] K. A. Fichthorn and W. H. Weinberg, J. Chem. Phys. **95**, 1090 (1991).
[15] A. Chatterjee and D. Vlachos, J. Comput.-Aided Mater. Des. **14**, 253 (2007).
[16] C. S. Becquart and C. Domain, Phys. Status Solidi B **247**, 9 (2010).
[17] F. Soisson and C.-C. Fu, Phys. Rev. B **76**, 214102 (2007).
[18] M. Y. Lavrentiev, R. Drautz, D. Nguyen-Manh, T. P. C. Klaver, and S. L. Dudarev, Phys. Rev. B **75**, 014208 (2007).
[19] S. Schmauder and P. Binkele, Comput. Mater. Sci. **24**, 42 (2002).
[20] G. Henkelman and H. Jónsson, J. Chem. Phys. **115**, 9657 (2001).
[21] F. El-Mellouhi, N. Mousseau, and L. J. Lewis, Phys. Rev. B **78**, 153202 (2008).
[22] D. Konwar, V. J. Bhute, and A. Chatterjee, J. Chem. Phys. **135**, 174103 (2011).
[23] H. Xu, R. Stoller, L. K. Béland, and Y. N. Osetsky, Comput. Mater. Sci. **100**, 135 (2015).
[24] N. Castin and L. Malerba, J. Chem. Phys. **132**, 074507 (2010).
[25] N. Castin, M. Pascuet, and L. Malerba, J. Chem. Phys. **135**, 064502 (2011).
[26] N. Castin, J. Fernandez, and R. Pasianot, Comput. Mater. Sci. **84**, 217 (2014).
[27] G. Bonny, R. Pasianot, and L. Malerba, Philos. Mag. A **89**, 3451 (2009).
[28] S. Curtarolo, G. L. W. Hart, M. B. Nardelli, N. Mingo, S. Sanvito, and O. Levy, Nat. Mater. **12**, 191 (2013).
[29] J. Behler and M. Parrinello, Phys. Rev. Lett. **98**, 146401 (2007).
[30] J. Behler, Phys. Chem. Chem. Phys. **13**, 17930 (2011).
[31] N. Artrith and J. Behler, Phys. Rev. B **85**, 045439 (2012).
[32] A. P. Bartók, M. C. Payne, R. Kondor, and G. Csanyi, Phys. Rev. Lett. **104**, 136403 (2010).
[33] W. J. Szlachta, A. P. Bartók, and G. Csányi, Phys. Rev. B **90**, 104108 (2014).
[34] J. Behler, J. Phys.: Condens. Matter **26**, 183001 (2014).
[35] N. Artrith and A. M. Kolpak, Nano Lett. **14**, 2670 (2014).
[36] L. Messina, N. Castin, C. Domain, and P. Olsson, Phys. Rev. B **95**, 064112 (2017).
[37] K. Binder, *Monte Carlo Methods in Statistical Physics* (Springer-Verlag, Berlin, Heidelberg, 1986), Chap. 1.
[38] J. Behler, J. Quantum Chem. **115**, 1032 (2015).
[39] A. Bartók and G. Csányi, J. Quantum Chem. **115**, 1051 (2015).
[40] M. C. Payne, M. P. Teter, D. C. Allan, T. A. Arias, and J. D. Joannopoulos, Rev. Mod. Phys. **64**, 1045 (1992).
[41] G. Henkelman and H. Jónsson, J. Chem. Phys. **113**, 9901 (2000).
[42] G. Henkelman and H. Jónsson, J. Chem. Phys. **113**, 9978 (2000).
[43] C. M. Bishop, *Neural Networks for Pattern Recognition* (Clarendon, Oxford, 1995).
[44] A. P. Bartók, R. Kondor, and G. Csányi, Phys. Rev. B **87**, 184115 (2013).
[45] G. Kresse and J. Hafner, Phys. Rev. B **47**, 558 (1993).
[46] G. Kresse and J. Hafner, Phys. Rev. B **49**, 14251 (1994).
[47] G. Kresse and J. Hafner, J. Phys.: Condens. Matter **6**, 8245 (1994).
[48] P. E. Blöchl, Phys. Rev. B **50**, 17953 (1994).
[49] G. Kresse and D. Joubert, Phys. Rev. B **59**, 1758 (1999).
[50] J. P. Perdew, K. Burke, and M. Ernzerhof, Phys. Rev. Lett. **77**, 3865 (1996).
[51] S. H. Vosko, L. Wilk, and M. Nusair, Can. J. Phys. **58**, 1200 (1980).
[52] D. Terentyev, N. Castin, and C. J. Ortiz, J. Phys.: Condens. Matter **24**, 475404 (2012).
[53] R. Pasianot and L. Malerba, J. Nucl. Mater. **360**, 118 (2007).
[54] P. Olsson, J. Wallenius, C. Domain, K. Nordlund, and L. Malerba, Phys. Rev. B **72**, 214119 (2005).
[55] G. Bonny, R. Pasianot, E. Zhurkin, and M. Hou, Comput. Mater. Sci. **50**, 2216 (2011).
[56] G. Bonny, D. Terentyev, and L. Malerba, Scr. Mater. **59**, 1193 (2008).
[57] G. Bonny, R. Pasianot, L. Malerba, A. Caro, P. Olsson, and M. Lavrentiev, J. Nucl. Mater. **385**, 268 (2009).
[58] N. Castin, L. Malerba, G. Bonny, M. I. Pascuet, and M. Hou, Nucl. Instrum. Methods Phys. Res. B **267**, 3002 (2009).
[59] P. Olsson, T. P. C. Klaver, and C. Domain, Phys. Rev. B **81**, 054102 (2010).
[60] H. C. Kang and W. H. Weinberg, J. Chem. Phys. **90**, 2824 (1989).
[61] S. Novy, P. Pareige, and C. Pareige, J. Nucl. Mater. **384**, 96 (2009).
[62] S. Novy, Mécanismes de vieillissement très longue chance des aciers inoxydables austnoferritiques, Ph.D. thesis, University of Rouen, France, 2009.
[63] V. Jacquet, Effet de l'irradiation sur la démixtion des alliages modèles FeCr autour de 15% de Cr, Ph.D. thesis, École Polytechnique, France, 2000.
[64] F. Bley, Acta Metall. Mater. **40**, 1505 (1992).
[65] C. Pareige, P. Pareige, B. Radiguet, and G. DaCosta, Private communication in the framework of the acknowledged FP7/NUGENIA-PLUS APLUS project.
[66] E. Martínez, O. Senninger, C.-C. Fu, and F. Soisson, Phys. Rev. B **86**, 224109 (2012).
[67] J. Hyde, G. DaCosta, C. Hatzoglou, H. Weekes, B. Radiguet, P. Styman, F. Vurpillot, C. Pareige, A. Etienne, G. Bonny, N. Castin, L. Malerba, and P. Pareige, Microsc. Microanal. **23**, 366 (2017).